RSC Advances

ROYAL SOCIETY
OF **CHEMISTRY**

www.rsc.org/advances

ARTICLE TYPE

Preparation and electrochemical characteristics of electrospun water-soluble resorcinol/phenol-formaldehyde resin-based carbon nanofibers

Xiaodong Tian,[a,b] Ning Zhao,[a] Kai Wang,[a,b] Defang Xu,[a,b] Yan Song,*[a] Quangui Guo,[a] and Lang Liu[a]

A series of flexible and free-standing carbon nanofiber mats derived from water-soluble resorcinol/phenol-formaldehyde resin/polyvinyl alcohol blend solution containing KOH were prepared by combining electrospinning and one-step carbonization/activation for the first time. Resultant porous carbon nanofibers have high specific surface area with large fraction of micropores ranging from 0.6 to 10 1.2 nm. The pore structure and chemical properties could be easily tuned by adjusting the amount of KOH. These carbon materials were studied as free-standing electrodes for supercapacitance eliminating the need for binding agents and conductive additives. The harshest activated sample with medium specific surface area (1169 m^2 g^{-1}) exhibited the largest specific capacitance of up to 332 F g^{-1} and the highest energy density about 37.6 Wh kg^{-1} at 0.1 A g^{-1}, about 59 % higher than those of the sample without activation 15 (209 F g^{-1}, 23.6 Wh kg^{-1} at 0.1 A g^{-1}). Furthermore, the specific capacitance could still remain 221 F g^{-1} at 20 A g^{-1} with the retention of 67 %. The sample also showed excellent cycle stability with 95 % capacity retention after 3000 cycles. The outstanding performance of activated porous carbon nanofibers could be attributed to the synergistic effect of the proper pore size distribution, high effective surface area and reasonable amount of oxygen-containing functional groups, resulting in both electrochemical double layer 20 and faradaic capacitance contributions.

Introduction

Supercapacitors are regarded as the most promising energy storage and power output devices for portable electronics, electric vehicles and renewable energy system,[1-4] due to its high power 25 density, fast charge/discharge rate, long cycle life, wide operational temperature range, high coulombic efficiency and improved safety.[5] These devices usually require electrode materials with tailored porosity, highly effective specific surface area (SSA) and suitable surface chemical properties. Therefore, a 30 breakthrough in electrode materials holds promise for fundamental advances in supercapacitor materials. Recently, nanostructured carbon materials with high SSA, excellent physicochemical stability, fine conductivity, proper pore size distribution (PSD), surface groups and acceptable cost have been 35 developed with the aim to improve the performance of supercapacitors.[6-8] This kind of materials can not only provide more ion adsorption or active sites for the formation of electrical double layer and charge transfer reactions, but also shorten diffusion and transport pathways for electrolyte ions during the 40 charge/discharge process.[8-11] Various strategies, including template method,[12] activation method[13], sol-gel method[14] and electrospinning technique,[15] have been developed to prepared nanostructured carbon materials. These carbonaceous materials exist in various forms, such as powders, monoliths, thin films, 45 fibers, papers, etc.. Among them, carbon papers or carbon mats

are beneficial in enhancing electrochemical characteristics due to the highly effective SSA, short diffusion length, structure integrity and conductive pathways. More importantly, they can be fabricated into free-standing electrode materials without the 50 addition of polymeric binding agents and conductive additives, thereby increasing the mass fraction of the active materials in a supercapacitor cell and improving the energy density.

By virtue of its simple procedure, low-cost and scale-up potential, electrospinning followed by simple thermal treatment has been 55 one of the hot issues in recent years.[15-17] Polyacrylonitrile (PAN),[18] polybenzimidazol (PBI),[19] polyaniline (PANI),[20] etc. have been electrospun to produce carbon nanofibers (CNFs). The electrospun CNFs with ultrathin diameters are typically arranged in interconnected non-woven network, which can provide good 60 mechanical integrity and an ideal framework for further surface modification.[18, 21, 22] Unfortunately, the capacitance performances of the CNF electrodes derived from these precursors are not good enough even though they have hierarchical pore structure and some extent of functional groups.[12-24] One of the problems is that 65 the pore sizes are not suitable for energy storage in aqueous electrolyte. Largeot, Chmiola, Raymundo-Piñero et al. have revealed that the pores with size of 0.6-1.2 nm are optimal for improving capacitance in aqueous electrolyte.[25-27] Therefore, fabricating nanostructured materials with more pores in 0.6-1.2 70 nm and a certain amount of functional groups through a sample method should be an effective route to improve the capacitance in aqueous electrolyte.

Herein, the water-soluble resole-type resorcinol/phenolic resin (PRF) was synthesized in polyvinyl alcohol (PVA) solution, yielding a PRF/PVA blend. The addition of the PVA can not only lead to good spinnability, but also act as a sacrificial template to some extent. Porous carbon nanofibers (PCNFs) prepared by electrospinning this blend solution containing KOH has been simultaneously carbonized and activated by one-step thermal treatment for the first time. The SSA, PSD and surface chemistry can be easily tuned by changing the content of KOH in the spinning solution. The synthesized samples exhibit excellent capacitive property when adopted as supercapacitor electrodes without the use of any conductive additives or binder.

Experimental

Materials

PVA (Mw =80 000) and resorcinol were purchased from the Sinopharm Chemical Reagent Company. Phenol, formaldehyde (37 wt. % aqueous solution), sodium hydroxide (NaOH), potassium hydroxide (KOH) and hydrochloric acid (HCl) were purchased from Tianjin Beichen Fangzheng Chemical Reagent Factory. All the chemical reagents in this work were of analytical grade and used without further purification.

Synthesis of spinning solution

The water-soluble resole-type PRF/PVA precursors for spinning were synthesized as follows: firstly, 2.5 g PVA was dissolved in 22.5 g distilled water to form 10 wt. % PVA aqueous solution. Then, the PVA solution was charged into a three-neck flask, which was equipped with a reflux condenser. Secondly, 5.55 g phenol, 1.62 g resorcinol and 0.89 g NaOH were added into the solution successively. Afterwards, the mixture was heated to 90 ^{o}C under vigorously stirring, and then 6.6 mL formaldehyde was added, the reaction was kept at 90 ^{o}C for 60 min. After that, 1.7 mL formaldehyde was added. The polymerization was ceased after 80 min. Subsequently, the as-synthesized solution was diluted to 20 wt. % in solid content with distilled water. In order to achieve good comparability, all the spinning parameters and solution concentration, excluding the content of KOH, were maintained the same. The KOH content, in the form of KOH/solid content mass ratio, was 0, 5, 8, 10, 15 wt. %.

Preparation of carbon nanofibers

The polymer solutions were spun into fiber mats through a positively charged capillary using an electrospinning apparatus (Shenzhen Tongli Micro & Nano Technology Co. Ltd., China), and the fibers were collected by a negatively charged stainless steel mesh. Electrospinning was carried out with a spinning distance of 15 cm at 10 kV under 28 ^{o}C and the solution feed rate was 1 mL h^{-1}.

The as-electrospun fibers were cured under 150 ^{o}C in air for 2 h followed by carbonization in a tube furnace at 800 ^{o}C for 3 h under argon flow with a heating rate of 5 ^{o}C min^{-1}. All obtained CNFs were repeatedly rinsed with 0.5 M HCl and distilled water to remove alkali metal compounds until the filtrate was neutral. The obtained CNFs with different amounts of KOH were denoted as PCNF-K-X, where X was the mass ratio of KOH/ solid content.

Characterization

The morphology of CNFs was investigated by field emission scanning electron microscope (FESEM, Hitachi S4800, Japan). ImageJ software was used for analysing the diameter distribution of fibers. The viscosity of the spinning solutions was carried out on a rheometer (DV-ⅢULTRA, BROOKFIELD, United States). The nanostructure of the samples was examined by a high resolution transmission electron microscopy (TEM, JEM-2010, Japan). The conductivity of the spinning solution was measured by a conductivity meter (DDS-307A, Shanghai Precision Scientific Instrument Co. Ltd., China) at room temperature. Characterization of the porous texture was conducted by physical adsorption of N_2 at 77 K using an automatic adsorption system (ASAP2020, Micromeritics, USA). The specific surface area and pore volume of PANF-K-Xs were calculated by Brunauer-Emmett-Teller (BET) and t-plot method. The nonlocal density functional theory (NLDFT) model was used to obtain the pore size distribution. X-ray photoelectron spectroscopy (XPS) measurements were performed using a AXIS ULTRA DLD spectrometer with a monochromated Al Kα radiation (hν = 1486.6 eV).

Electrochemical measurements

All electrochemical tests were performed on CHI 660C instrument (Shanghai Chenhua Apparatus Co. Ltd., China) at room temperature by using a three-electrode configuration. A platinum sheet and Hg/HgO electrode were used as counter electrode and reference electrode, respectively. The PCNF mats were directly cut into 1 × 1 cm square and then pressed between two pieces of nickel foams in the same area to form a working electrode. The measurements were carried out in 6 M KOH aqueous electrolyte at room temperature. All cyclic voltammetry (CV) curves were collected with a potential window from – 0.9 to 0 V at different scan rates. Galvanostatic charge/discharge (GCD) curves were measured at different current density from 0.1 to 20 A g^{-1}. Electrochemical impedance spectra (EIS, frequency range from 0.01 Hz to 100 kHz, amplitude of 5 mV at open circuit potential) were also measured. The cycling stability test was evaluated by a Land CT2001A battery program control test system (LAND, Wuhan, China).

Results and discussion

Microstructure characterization

The SEM images of the PCNF-K-Xs and the corresponding diameter distributions with different KOH concentration are shown in Fig. 1. All samples exhibit regular fibrous morphology with different diameters and stack randomly to form a network structure. Along with the increase of KOH content, the average diameter of the fibers decreases gradually from 457 to 296 nm and the surface of fibers becomes increasingly rough (the insets of Fig. 1). Since electrospinning was carried out under similar viscosity (Fig. S1), these differences should be attributed to the changes of the electrical conductivity of the spinning solution and the etching reactivity of KOH with carbon species. As shown in Fig. 2, the electrical conductivity of the solution arises when the content of KOH increased. It should be noted that when the KOH content is up to 15 wt. %, some incomplete splits are observed, which are consistent with previous reports.[21, 28] One of the reasons is that a large quantity of charges on the negative plate

influences the bending stability of the spinning solution, which leads to incompleted split.[29-31] The TEM images of both longitudinal section and cross-section of PCNF-K-15 show a clear internal porous structure. The pores are interconnected with the carbon domains (Fig. 3).

Fig. 1 SEM images of the PCNF-K-Xs: (a) PCNF-K-0, (b) PCNF-K-5, (c) PCNF-K-8, (d) PCNF-K-10, (e) PCNF-K-15 and (f) the corresponding diameter distributions.

Fig. 2 Change of the conductivity of the spinning solution with different KOH content.

Fig. 3 The TEM images of longitudinal section (a) and cross-section (b) of PCNF-K-15.

Nitrogen adsorption-desorption isotherms were used to investigate the effects of the content of KOH on the pore structure and SSA. All samples exhibit typical Ⅰ isotherm according to the International Union of Pure and Applied Chemistry (IUPAC) classification, which is indicative of a typical microporous material (Fig. 4a). Compared with PCNF-K-0, activated samples display more increment in nitrogen adsorption capacity in the entire relative pressure region, implying more pores in these samples. Fig. 4b shows that the samples without activation possesses abundant micropores in the narrow size range of 0.6-0.9 nm, while the samples treated with KOH have a large fraction of micropores (mainly in four regions: 0.6-0.9, 1.1-1.3, 1.5-1.9) and newly developed mesopores ranging from 2.0 to 2.4 nm, representing three levels of micropores and small mesopores, respectively. Both these pores play an important role in charge accumulation. Micropores are responsible for charge storage and ion adsorption, especially for the micropores with

pore sizes less than that of the solvated electrolyte ion size.[25] While mesopores function as channels for ions transmission, improving the accessibility of micropores to electrolytes. The textural characteristics of PANF-K-Xs are listed in Table 1. It can be seen that the SSA and total pore volume of the samples increase first and then decrease when the content of KOH increases from 0 to 15 wt. %. It might be explained as follows: when the KOH content is relatively low, KOH lead to more pores by the release of gases due to the reaction of KOH and carbon, as well as by K deintercalation in pesudographitic layers.[32-34] However, when the concentration of KOH continues to increase, the excess KOH will further etch the skeleton carbon around micropores, resulting in coalescing pore walls. In addition, few mesopores in the size range of 2.0-2.4 nm makes little contribution to the enhancement of SSA and pore volume, so PCNF-K-10 and PCNF-K-15 have similar surface area and total pore volume.

Fig. 4 Nitrogen adsorption/desorption isotherms (a) and pore size distributions of PCNF-K-Xs (b).

Table 1 Textural characteristics and element composition by XPS of PCNF-K-Xs

Smaple	Textural characteristics				Element composition by XPS (at.%)	
	$S_{BET}{}^{a}$ $(m^2\,g^{-1})$	$V_{total}{}^{b}$ $(cm^3\,g^{-1})$	$S_{micro}{}^{c}$ $(m^2\,g^{-1})$	$V_{micro}{}^{d}$ $(cm^3\,g^{-1})$	C	O
PCNF-K-0	653	0.28	587	0.23	96.15	3.85
PCNF-K-5	911	0.40	788	0.31	94.34	5.66
PCNF-K-8	1292	0.56	1060	0.42	91.74	8.26
PCNF-K-10	1161	0.52	957	0.38	90.09	9.91
PCNF-K-15	1169	0.51	970	0.39	88.49	11.51

[a] Total surface area calculated using the BET method. [b] Total pore volume calculated at $P/P_0 = 0.995$. [c] Micropore surface area calculated from *t*-plot method. [d] Micropore volume derived from *t*-plot method..

The increasing mass ratio of KOH/solid content not only results in somewhat more developed porosity, but also affects significantly the surface functionality. The XPS measurements reveal that oxygen-containing functionalities exist in all samples, which are considered to effectively enhance the hydrophilicity and wettability of PCNF-K-Xs in aqueous eletrolytes. Compared with PCNF-K-0, the O content of the materials increases from 3.85 to 11.51 at.% after activation (Table 1). The C 1s and O 1s peaks of the scan spectra have binding energy of ca. 284.6 and 533.5 eV, respectively (Fig. 5a). High resolution XPS measurements were performed to investigate the atomic binding states of the prepared CNFs. In case of C 1s, four different groups of C=C/C-C in sp[2]-hybridized domains, C-O (phenolic, hydroxyl or ether), C=O (carbonyl or quinone groups) and O=C-O (carboxyl groups) are determined by the peaks at 284.5, 285.7, 286.6, 288.9 eV, respectively (Fig. 5b). The chemical state of

oxygen atoms could also be assigned to four peaks at 531.3, 532.3, 533.3, and 535.2 eV, which can be attributed to C=O (carbonyl and/or quinone), C-OH/C-O-C (hydroxyl and ether), O-C=O (carbonyl), chemisorbed oxygen and/or water (Fig. 5c).[35-37] Content of each carbon and oxygen component are shown in Table 2. It can be found that the samples treated with different concentrations of KOH lead to an increase in the changes in their distribution as well as the content of surface oxygen functional groups. The content of C=O and O=C-O increase slightly at the expense of C-O or C-O-C groups, which is in accordance with the content analysis results of carbon components.

Electrochemical characterizations

The electrochemical performance of the supercapacitor electrode was evaluated in a three-electrode setup. Typical CV curves at a scan rate of 5 mV s^{-1} for all samples are presented in Fig. 6a. It shows that all the CV curves are slightly distorted rectangular shapes with small, broad hump at low potential, which means the co-contribution of electrochemical double layer capacitance arising from charge separation at the interface of electrode/electrolyte and pseudo-capacitance arising from quick faradic reactions related to surface functionalities in the carbon matrix.

Fig. 5 (a) X-ray photoelectron spectra, (b) the C 1s, (c) the O 1s of all samples

Table 2 Peak assignment of C 1s, O 1s for the prepared samples

Peak	Binding energy (eV)	Assignment	Fraction of species (%)				
			PCNF-K-0	PCNF-K-5	PCNF-K-8	PCNF-K-10	PCNF-K-15
C 1s	284.5	sp^2 C-C	75.23	75.91	73.63	71.8	71.11
	285.7	C-O/C-C	8.76	9.19	9.9	8.79	8.33
	286.6	C=O	7.71	7.13	8.24	9.11	9.38
	288.9	O=C-O	8.3	7.77	8.23	10.3	11.18
O 1	531.3	C=O	34.19	33.87	31.54	32.95	34.93
	532.3	C-OH/O-C-O	31.11	31.51	29.28	39.19	27.05
	533.3	O-C=O	26.89	27.41	32.86	29.83	29.92
	535.2	Chemisorbed oxygen/water	7.81	7.21	6.32	7.03	8.10

Generally, the oxygen-containing functional groups are commonly formed by carbonization and activation.[38] These oxygen-containing functionalities can not only provide pseudo-capacitance by introducing electro-acceptor properties into the carbon surface,[39] but also improve the wettability of surface to enhance the ion diffusion and surface utilization in aqueous solution.[40, 41] Given the small quantity of proton in 6 M KOH, the O Ⅰ is no longer electrochemically active, which was confirmed by several publications.[42, 43] However, the C=O groups can further improve the wettability of the carbon surface and reduce the charge transfer resistance. Meanwhile, the O-C=O groups can exhibit quasi-reversible pseudo-capacitance by deprotonation.[44-46] Fortunately, the percentage of C=O and O-C=O exceed over 60% of the total O species (Table 2), which will make a great contribution to the total capacitance of obtained electrodes. In Fig. 6b, the slightly distorted rectangular shape can even be kept when the sweep rate is up to 100 mV s^{-1}. It reveals that the samples, especially for PCNF-K-15, have excellent ionic accessibility, which suggests that it is more suitable for quick charge/discharge operation. In order to prove this point of view, CV measurements

Fig. 6 CV curves for all samples at scan rate of 5 mV s^{-1} (a) and 100 mV s^{-1} (b).

at scan rate from 5 to 200 mV s^{-1} were carried out and the results are illustrated in Fig. S2. The quasi-rectangular shape is well maintained at the scan rate of 200 mV s^{-1}, probably due to a 3D network with developed pore structure for electronic transmission and electrolyte infiltration, which would improve the electrochemical utilization during the charge/discharge process. GCD measurements were performed in the voltage range of -0.9-0 V. As seen in Fig. S3, the shape of the discharge curve is like an arc line, which is related to pseudo faradic reactions. The

redox reactions are more obvious in the discharge curves of PCNF-K-15 (Fig. S4), which is consistent with the trend obtained from CV results. Despite the maximum SSA for PCNF-K-8 sample, the electrochemical performance is not the best,
[5] demonstrating that the capacity is not proportional to SSA, which is consistent with previous researches.[23, 43, 47] The increase in capacitance between PCNF-K-15 and PCNF-K-10 is more prominent (~ 13%) than the corresponding rise in the SSA (~ 0.7%), also suggesting that the SSA is not the only factor
[10] determining capacitance. Since PCNF-K-8, PCNF-K-10 and PCNF-K-15 have similar PSD, the different performances should be caused by the differences of the content of oxygen functional groups and the fiber diameters, which are beneficial to improving the surface utilization in aqueous solution and shortening the ion
[15] diffusion length, respectively. No obvious internal resistance drop (IR drop, 0.01-0.02 V) can be observed even at the current density of 5 A g^{-1} (Fig. 7a), indicating a low resistance and good power property of these materials, which can be attributed to the large fractions of C=O groups. To further understand the rate
[20] capability of PCNF-K-X electrodes, the charge/discharge measurements at different current densities were recorded. The specific capacitance was calculated from the slope of the discharge curve, according to the Eq. (1)

$$C = (I \times \Delta t)/(\Delta V \times m) \qquad (1)$$

[25] where C is the specific capacitance (F g^{-1}), I is the constant discharge current (A), Δt is the discharge time (s), ΔV is the voltage difference in discharge (V) and m is the mass of the active materials (g).
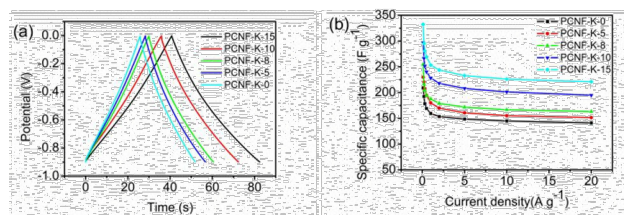

[30] **Fig. 7** Galvanostatic charge/discharge curves at 5 A g^{-1} (a); gravimetric capacitances measured at various charge/discharge current density (b).

The specific capacitance decreases gradually with the increase of current density. But all the activated samples exhibit higher capacitance and higher capacitance retention (~67 %) with the
[35] increase in current density from 0.1 to 20 A g^{-1} (Fig. 7b). Two factors may lead to this result: firstly, the samples treated with KOH possess higher O content than that of PCNF-K-0, which provides large additional pseudo-capacitance; secondly, the presence of small size mesopores in activated samples favor the
[40] charge transfer process and ion diffusion. Among these samples in this work, PCNF-K-15 shows the highest capacitance (332 F g^{-1} at 0.1 A g^{-1}), and the specific capacitance could still remain 221 F g^{-1} at 20 A g^{-1}, indicating that it allows rapid ion diffusion, partially because of the short charge transport distance, benefiting
[45] from the short average fiber diameter and proper PSD. These observations are in good agreement with the quasi-rectangular shapes of CV curves of all activated samples at high scan rate.
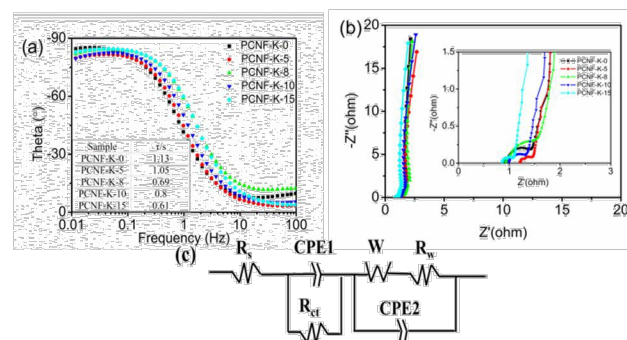

[50] **Fig. 8** Bode plots and their corresponding time constants of all samples (a), Nyquist plots of all samples (b). the equivalent circuit for simulating the impedance spectra (c).

RC time constant, which was marked as τ, is another important index to evaluate the performance of supercapacitors. It is the
[55] reciprocal of - 45° of corresponding frequency and it represents how fast the capacitor can be charged and discharged.[48] As seen from Fig. 8a, all electrodes show smaller time constant, ranging from 0.61 to 1.13 s, than that of previous literature,[49] suggesting lower resistance attributed to the optimized PSD and oxygen
[60] functional groups in the obtained samples. In general, narrow micropores will only be accessed through an appreciable resistance arising from restricted electrolyte diffusion, which will contribute directly to a high time constant.[50] As shown in Fig. 4b and Fig. 8a, PCNF-K-0, with the narrowest micropores, has the
[65] highest RC time constant. It also can be proved by the EIS diagram in Fig. 8b, all impedance spectra are almost similar with a quasi-semicircle at high frequency region and a line at low frequency region. The almost vertical lines at low frequencies correspond to the capacitive response of porous carbons. The
[70] more vertical the line is, the more closely the supercapacitor behave as an ideal capacitor. Compared with other samples, PCNF-K-15 electrode shows the straightest line, which means the best capacitive behavior. Clearly, the internal resistance of PANF-K-15 is the lowest among all samples. In order to get
[75] insight into the information contained in the impedance plot, a fitting equivalent circuit model is displayed in Fig. 8c. The whole capacitor circuit is constituted by the bulk electrolyte resistance (R_s), two constant phase elements (CPE) representing the non-ideal capacitor behavior, the Warburg impedance (W), the charge
[80] transfer resistance (R_{ct}) and the diffusion resistance (R_w). The impedance of the CPE and the Warburg element W are given in Eq. (2) and Eq. (3), respectively.

$$Z = 1/T(i\omega)^p \qquad (2)$$

where T is the magnitude and p the exponent.

[85] $$W = R_w \coth[IT_W\omega]^{W_p}/(IT_w\omega)^{W_p} \qquad (3)$$

where R_w is the diffusion resistance, $T_w = 2L/D$, L is the diffusion length, D is the diffusion coefficient and W_p is the exponent (between 0 and 1). The parameters calculated from the fitting of the equivalent circuit in Fig. 8c are shown in Table 3. A
[90] good fit was obtained in experiments, which is consistent with the RC time constant.

ARTICLE TYPE

Table XX Caption

Samples	$R_s(\Omega)$	$R_{ct}(\Omega)$	$T_1/10^{-3}$	P_1	$R_w(\Omega)$	T_w	W_p	T_2	P_2
PCNF-K-0	1.22	0.53	8.73	0.81	5.97	0.15	0.91	0.14	0.90
PCNF-K-5	1.12	0.68	9.67	0.83	8.21	0.09	0.89	0.13	0.91
PCNF-K-8	0.94	0.23	6.84	0.80	10.78	0.09	0.92	0.07	0.90
PCNF-K-10	0.99	0.38	9.24	0.81	28.46	0.10	0.99	0.11	0.91
PCNF-K-15	0.86	0.21	5.79	0.88	28.69	0.11	0.96	0.12	0.92

Long cycle life is another important factor to determine the performance of a supercapacitor. Fig. 9a shows the cycling property of PCNF-K-15 under the current density of 2 A g^{-1}. It 5 can be seen that the sample shows high capacitance retention over 95 % after 3000 cycles, demonstrating its good cycle stability. This is because CNFs prepared by electrospinning can facilitate the transport of electrolyte ions within the particles and also improve the effective electrochemical utilization of active 10 materials. Importantly, these CNFs can effectively buffer the stress from the expansion and shrinkage of the electrodes during the process of charge/discharge, which could prevent the pulverization of electrode and improve the cycle stability.[52] The capacitance loss may be ascribed to self-discharge caused by the 15 surface oxygen retention. The extent of surface oxygen retention, as physically adsorbed molecular oxygen or as surface complexes, is believed to influence the mechanism of capacitor self-discharge, which is related to the cycle stability. Ragone plots, relating the energy density to the power density, as an efficient way to 20 evaluate the capacitive performance of supercapacitors, have also been used to characterize the electrode materials.[53, 54] To determine the operational characteristics, the energy density (E, Wh kg^{-1}) at different power density (P, W kg^{-1}) of PCNF-K-Xs electrode was calculated average from GCD curves at different 25 discharge current densities to the following equations:

$$E = C\Delta V^2/2 \tag{4}$$

$$P = E/t \tag{5}$$

where C, ΔV, t are indicating of the specific capacitance (F g^{-1}), 30 discharge curves excluding initial drop (V) and discharge time (s), respectively. The Ragone plots are displayed in Fig. 9b. The samples treated with KOH show obviously improved energy density than that of pristine CNFs. The sample PCNF-K-15 exhibits the highest energy density (~ 37.6-24.8 Wh kg^{-1}) among 35 all samples in this work. Furthermore, the energy density of PCNF-K-15 electrode is much higher than those of highly corrugated graphene sheets (~30.4 Wh kg^{-1}),[54] chemically converted graphene/onion-like carbon (~20 Wh kg^{-1}),[55] and chemically reduced graphene (~11.5 Wh kg^{-1}).[56] For a symmetric 40 supercapacitor composed of two identical PCNF-K-X electrodes, the specific capacitance would be one-fourth of that of a single electrode in a three-electrode cell. Taking into account the specific capacitance of the capacitor discharged in the operating voltage of -0.9-0 V, a practical energy density of 9.4 Wh kg^{-1} is

45 obtained. The superior performance of the PCNF-K-15 electrode is attributed to the following reasons: (1) the electrospun fiber mats have high accessible SSA, short diffusion length and integrate conductive pathways, which are favorable to providing more active sites for energy storage and speedy charge 50 transmission; (2) optimized PSD can enhance the transportation of electrolyte ions. Micropores are responsible for charge storage and ion adsorption, especially when micropores have pore sizes ranging from 0.6-1.2 nm, while mesopores function as channels for ions transportation, improving the accessibility of micropores 55 to electrolytes; (3) the transformation of the surface states on the CNF surfaces improves the capacitance property by improving the wettability of carbon surface and introducing electro-acceptor properties to enhance the contact area between material surface and electrolyte and provide pseudo-capacitance contribution.

60 **Fig. 9** Cycling stability of PCNF-K-15 at a current density of 2 A g^{-1} up to 3000 cycles (a) and Ragone plots of the PCNF-K-X (X=0, 5, 8, 10, 15) electrodes (b).

Conclusions

65 Activated porous carbon nanofibers mats were prepared by electrospinning water-soluble resole-type PRF/PVA blend solution, followed by one-step activation. The amount of KOH in the spinning solution is a key factor affecting the fiber diameter, specific surface area, pore volume, pore size distribution, and 70 surface chemistry. Activated samples have a large fraction of micropores ranging from 0.6 to 1.2 nm and a certain number of small mesopores in the size range of 2.0-2.4 nm. The PCNF-K-15 has maximal specific capacitance (332 F g^{-1} at 0.1 A g^{-1}), excellent cycling stability (about 95 % retention of capacitance 75 after 3000 continuous cycles at 2 A g^{-1}), high rate ability (67 % from 0.1 to 20 A g^{-1}) and high energy density. The remarkable behavior of PCNF-K-Xs can be attributed to the combined effects of the optimized pore structures of electrospun CNFs electrode and the transformation of activated states on the PCNF-K-Xs. 80 Hence, these electrospun CNF electrode materials hold a

significant promise for applications as an efficient electrode material.

Acknowledgements

Notes and References

a Key Laboratory of Carbon Materials, Institute of Coal Chemistry, Chinese Academy of Sciences, Taiyuan 030001, China. Email: yansong1026@126.com; Fax: +86 351 2021135; Tel: +86 2021135.
b University of Chinese Academy of Sciences, Beijing 100049, China
† Electronic Supplementary Information (ESI) available: [Viscosity changes of the spinning solutions and some electrochemical properties of porous carbon nanofiber electrodes]. See DOI: 10.1039/b000000x/
‡ Footnotes should appear here. These might include comments relevant to but not central to the matter under discussion, limited experimental and spectral data, and crystallographic data.

1   A. Burke, *J. Power Sources* 2000, **91**, 37-50.
2   A. Chu and P. Braatz, *J. Power Sources*, 2002, **112**, 236-246.
3   L. L. Zhang and X. S. Zhao, *Chem. Soc. Rev.*, 2009, **38**, 2520-2531.
4   N. S. Choi, Z. Chen, S. A. Freunberger, X. Ji, Y. K. Sun, K. Amine, G. Yushin, L. F. Nazar, J. Cho and P. G. Bruce, *Angew. Chem. Int. Ed.*, 2012, **51**, 9994-10024.
5   M. Inagaki, H. Konno and O. Tanaike, *J. Power Sources*, 2010, **195**, 7880-7903.
6   P. Simon and Y. Gogotsi, *Nat. Mater.*, 2008, **7**, 845-854.
7   A. Ghosh and Y. H. Lee, *ChemSusChem*, 2012, **5**, 480-499.
8   A. Alonso, V. Ruiz, C. Blanco, R. Santamaría, M. Granda, R. Menéndez and S. G. E. De Jager, *Carbon*, 2006, **44**, 441-446.
9   P. Simon and Y. Gogotsi, *Acc. Chem. Res.*, 2012, **46**, 1094-1103.
10   E. Raymundo-Piñero, F. Leroux and F. Béguin, *Adv. Mater.*, 2006, **18**, 1877-1882.
11   W. Huang, H. Zhang, Y. Huang, W. Wang and S. Wei, *Carbon*, 2011, **49**, 838-843.
12   C. Liang, Z. Li and S. Dai, *Angew. Chem. Int. Ed.*, 2008, **47**, 3696-3717.
13   F. C. Wu, R. L. Tseng, C. C. Hu and C. C. Wang, *J. Power Sources*, 2005, **144**, 302-309.
14   J. Wang, X. Yang, D. Wu, R. Fu, M. S. Dresselhaus and G. Dresselhaus, *J. Power Sources*, 2008, **185**, 589-594.
15   P. Ramesh Kumar, N. Khan, S. Vivekanandhan, N. Satyanarayana, A. Mohanty and M. Misra, *J. Nanosci. Nanotechnol.*, 2012, **12**, 1-25.
16   R. Sahay, P. S. Kumar, R. Sridhar, J. Sundaramurthy, J. Venugopal, S. G. Mhaisalkar and S. Ramakrishna, *J. Mater. Chem.*, 2012, **22**, 12953-12971.
17   S. Cavaliere, S. Subianto, I. Savych, D. J. Jones and J. Rozière, *Energy Environ. Sci.*, 2011, **4**, 4761-4785.
18   G. Wang, C. Pan, L. Wang, Q. Dong, C. Yu, Z. Zhao and J. Qiu, *Electrochim. Acta*, 2012, **69**, 65-70.
19   C. Kim, S. H. Park, W. J. Lee and K. S. Yang, *Electrochim. Acta*, 2004, **50**, 877-881.
20   S. Chaudhari, Y. Sharma, P. S. Archana, R. Jose, S. Ramakrishna, S. Mhaisalkar and M. Srinivasan, *J. Appl. Polym. Sci.*, 2013, **129**, 1660-1668.
21   C. Kim, B. T. N. Ngoc, K. S. Yang, M. Kojima, Y. A. Kim, Y. J. Kim, M. Endo and S. C. Yang, *Adv. Mater.*, 2007, **19**, 2341-2346.
22   G. H. An and H. J. Ahn, *Carbon*, 2013, **65**, 87-96.
23   M. Teng, J. Qiao, F. Li and P. K. Bera, *Carbon*, 2012, **50**, 2877-2886.
24   C. Tran and V. Kalra, *J. Power Sources*, 2013, **235**, 289-296.
25   C. L. C. Portet, J. Chmiola, P. L. T. Y. Gogotsi and P. Simon, *J. Am. Chem. Soc.*, 2008, **130**, 2730-2731.
26   J. Chmiola, G. Yushin, Y. Gogotsi, C. Portet, P. Simon and P. L. Taberna, *Science*, 2006, **313**, 1760-1763.
27   E. Raymundo-Piñero, K. Kierzek, J. Machnikowski and F. Béguin, *Carbon*, 2006, **44**, 2498-2507.
28   C. Zhang, X. Yuan, L. Wu, Y. Han and J. Sheng, *Eur. Polym. J.*, 2005, **41**, 423-432.
29   A. L. Yarin, S. Koombhongse and D. H. Reneker, *J. Appl. Phys.*, 2001, **89**, 3018-3026.
30   D. H. Reneker, A. L. Yarin, H. Fong and S. Koombhongse, *J.Appl. Phys.*, 2000, **87**, 4531-4547.
31   S. A. Theron, E. Zussman and A. L. Yarin, *Polymer*, 2004, **45**, 2017-2030.
32   S. H. Yoon, S. Lim, Y. Song, Y. Ota, W. Qiao, A. Tanaka and I. Mochida, *Carbon*, 2004, **42**, 1723-1729.
33   M. A. Lillo-Ródenas, D. Cazorla-Amorós and A. Linares-Solano, *Carbon*, 2003, **41**, 267-275.
34   W. Qiao, S. H. Yoon and I. Mochida, *Energ. Fuel.*, 2006, **20**, 1680-1684.
35   S. Binak, G. Szymański, J. Siedlewski and A. Świątkowski, *Carbon*, 1997, **35**, 1799-1810.
36   D. Hulicova-Jurcakova, M. Seredych, G. Q. Lu and T. J. Bandosz, *Adv. Funct. Mater.*, 2009, **19**, 438-447.
37   R. Arrigo, M. Hävecker, S. Wrabetz, R. Blume, M. Lerch, J. McGregor, E. P. J. Parrott, J. A. Zeitler, L. F. Gladden, A. Knop-Gericke, R. Schlögl and D. S. Su, *J. Am. Chem. Soc.*, 2010, **132**, 9616-9630.
38   M. J. Bleda-Martínez, J. A. Maciá-Agulló, D. Lozano-Castelló, E. Morallón, D. Cazorla-Amorós and A. Linares-Solano, *Carbon*, 2005, **43**, 2677-2684.
39   H. Yang, M. Yoshio, K. Isono and R. Kuramoto, Electrochem. Solid St., 2002, 5, A141-A144.
40   C. T. Hsieh, W. Y. Chen and Y. S. Cheng, *Electrochim. Acta*, 2010, **55**, 5294-5300.
41   D. Qu, *J. Power Sources*, 2002, **109**, 403-411.
42   H. A. Andreas and B. E. Conway, *Electrochimica Acta*, 2006, **51**, 6510-6520.
43   D. Hulicova-Jurcakova, M. Kodama, S. Shiraishi, H. Hatori, Z. H. Zhu and G. Q. Lu, *Adv. Funct. Mater.*, 2009, **19**, 1800-1809.
44   L. Wan, J. Wang, Y. Sun, C. Feng and K. Li, *RSC Advances*, 2015, **5**, 5331-5342.
45   L. Jiang, J. Yan, L. Hao, R. Xue, G. Sun and B. Yi, *Carbon*, 2013, **56**, 146-154.
46   L. X. Li and F. Li, *New Carbon Mater.*, 2011, **26**, 224-228.
47   J. Chmiola, C. Largeot, P. L. Taberna, P. Simon and Y. Gogotsi, *Science*, 2010, **328**, 480-483.
48   B. E. Conway, *Electrochemical supercapacitors: Scientific Fundamentals and Technological Applications*, Kluwer Academic/Plenum Publishers, New York 1999.
49   P. L. Taberna, P. Simon and J. F. Fauvarque, *J. Electrochem. Soc.*, 2003, **150**, A292-A300.
50   A. G. Pandolfo and A. F. Hollenkamp, *J. Power Sources*, 2006, **157**, 11-27.
51   A. M. Al-Enizi, A. A. Elzatahry, A. M. Abdullah, M. A. AlMaadeed, J. Wang, D. Zhao and S. Al-Deyab, *Carbon*, 2014, **71**, 276-283.
52   J. Yan, Q. Wang, T. Wei and Z. Fan, *Adv. Energy Mater.*, 2013, DOI: 10.1002/aenm.201300816.
53   K. W. Nam, C. W. Lee, X. Q. Yang, B. W. Cho, W. S. Yoon and K.-B. Kim, *J. Power Sources*, 2009, **188**, 323-331.
54   J. Yan, J. Liu, Z. Fan, T. Wei and L. Zhang, *Carbon*, 2012, **50**, 2179-2188.
55   Y. Sun, Q. Wu, Y. Xu, H. Bai, C. Li and G. Shi, *J. Mater. Chem.*, 2011, **21**, 7154-7160.
56   S. Y. Yang, K. H. Chang, H. W. Tien, Y. F. Lee, S. M. Li, Y. S. Wang, J. Y. Wang, C. C. M. Ma and C. C. Hu, *J. Mater. Chem.*, 2011, **21**, 2374-2380.